

Non-stationary heat flux measurement in shock tube experiments using sensors based on anisotropic bismuth thermoelements

© P.A. Popov, N.A. Monakhov, T.A. Lapushkina, S.A. Poniaev

Ioffe Institute,
194021 St. Petersburg, Russia
e-mail: pavel.popov@mail.ioffe.ru

Received March 14, 2022

Revised April 23, 2022

Accepted May 4, 2022

An analysis of main features of unsteady heat flux measuring in shock tubes experiments with a characteristic process time of $\sim 1\ \mu\text{s}$ – $1\ \text{ms}$ using sensors based on anisotropic bismuth thermoelements is made. The heat flux behind the reflected shock wave and at the blunt body stagnation point has been measured. Testing of the heat flux calculation method was carried out. The difference between the experimental data and the theoretical value of the heat flux does not exceed 50%. The possible reasons influencing the magnitude of measurement uncertainty are analyzed. The experiments performed have shown the applicability of a sensor based on anisotropic thermoelements and the method for calculating the heat flux from its electrical signal for typical conditions of experiments on shock tubes.

Keywords: heat flux, shock tube, measurements, anisotropic thermoelement, ghfs.

DOI: 10.21883/TP.2022.09.54677.54-22

Introduction

Measuring the heat flux to the surface of a body flown by a high-enthalpy gas flow is the basic diagnostics in an aerophysical experiment, since it allows one to obtain an integral characteristic of heat transfer processes in the shock layer [1–3]. Under the conditions of a ground-based experiment, a fairly complete reproduction of the conditions of a real high-speed flight is possible only on pulsed gasdynamic facilities with an operating time of ~ 1 – $10\ \text{ms}$ [1,2,4,5]. Therefore, the main requirements for thermal sensors are high speed $\sim 1\ \mu\text{s}$ with a total recording duration of $\sim 10\ \text{ms}$ and a measurement range from $\sim 100\ \text{kW/m}^2$ to $\sim 10\ \text{MW/m}^2$. Also, stringent requirements are imposed on mechanical strength due to the force impact of a high-speed gas flow and the presence of fine solid particles in it [6].

The most widespread are sensors based on the temperature dependence of the electrical resistance of the sensitive element and thermoelectric sensors based on the Seebeck effect. The first type includes thin-film resistance sensors [7], and the second type includes coaxial thermocouples [8], sensors based on a thin anisotropic film of high-temperature superconductors [9,10] and chromium [11], as well as sensors based on anisotropic bismuth thermoelements and layered metal structures [12,13]. Until recently, thin-film resistance sensors were the main means of measurement. Due to the low mechanical strength of the metal film, they are not used at high enthalpies of the oncoming gas flow and have recently been practically replaced by coaxial thermocouples. Their main advantage is high mechanical strength. The disadvantages include a low electrical signal ~ 10 – $100\ \mu\text{V}$ and rather large dimensions. The

thermal inertia of the sensitive element of thin-film sensors and the need for mathematical signal processing based on the solution of a one-dimensional non-stationary heat conduction equation limits the upper frequency limit of the recorded heat flow. A distinctive feature of thermoelectric sensors based on anisotropic films $\sim 1\ \mu\text{m}$ thick is the rapid (~ 0.1 – $1\ \mu\text{s}$) establishment of a stationary temperature distribution in the sensitive element. For this reason, the electrical signal of the sensor is proportional to the heat flux passing through it, and the processing of the measurement results is come down to multiplying the signal recorded in the experiment by the known calibration coefficient [10,11].

Other approaches are also used in experiments on pulsed gasdynamic facilities, for example, applying heat-sensitive paints to the surface of the model and then taking high-speed photography during the experiment [14]. However, such methods are much more laborious and are used mainly for the qualitative analysis of the thermal effect of a high-enthalpy flow on the model surface.

In this work, we used a sensor based on anisotropic thermoelements developed at the St. Petersburg Polytechnic University [12]. It is a battery of bismuth thermoelements connected in series, fixed on a mica substrate and separated from each other by lamsan strips. The experience of using sensors of this type in various conditions has shown that they have a high electrical signal and noise immunity even under conditions of strong electromagnetic fields with sufficient mechanical strength [15–17].

In [18] a method for calculating the heat flux from the electrical signal of a single anisotropic thermoelement in a non-stationary thermal regime is proposed. It is based on a one-dimensional model of thermal and thermoelectric processes in thermoelements and is a cyclic solution of a

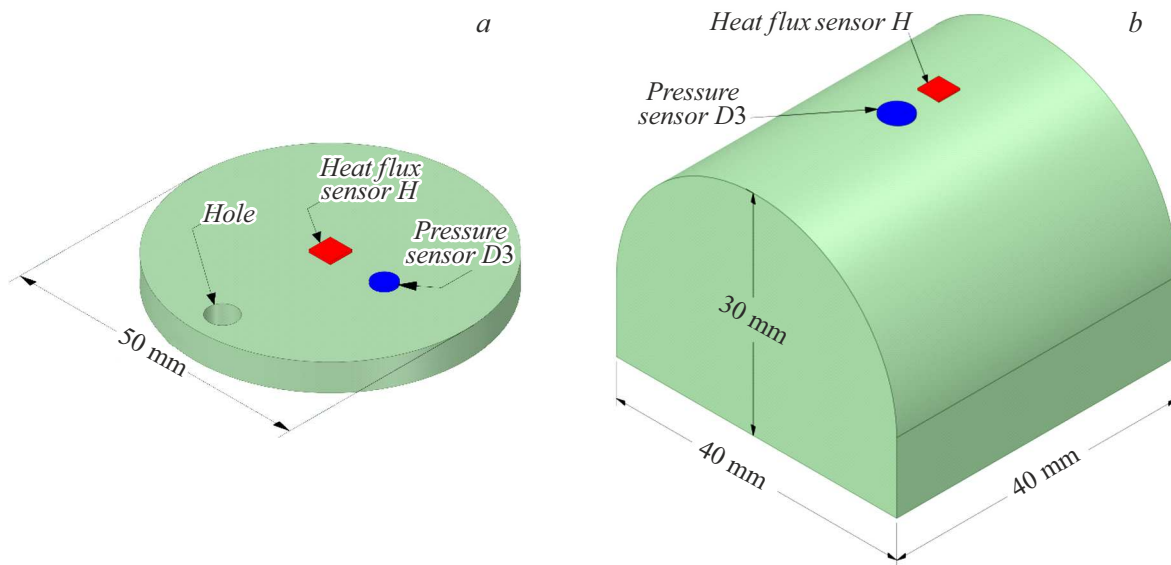


Figure 1. An end cap for measuring the heat flow behind the reflected shock wave (a) and a blunt body for measuring the heat flow at the critical point in a supersonic gas flow (b).

one-dimensional non-stationary heat equation with a special boundary condition. The main parameter affecting the uncertainty in calculating the heat flow from an electrical signal is the ratio of the length to the thickness of the thermoelement l/h . The performed calculations showed that when sensors with $l/h > 10$ are used, the uncertainty does not exceed 10%. An alternative method for processing measurement results, also based on a one-dimensional thermoelectric model, is proposed in [19].

The main objective of this work is to experimentally verify the method proposed in [18] and analyze its applicability in experiments on shock tubes. The heat flux was measured using sensors with different ratios l/h . Two classical gas-dynamic problems with significantly different characteristic times and a well-known theoretical solution were chosen as test problems: heat transfer with the wall in the stagnation region behind the reflected shock wave and heat transfer at the critical point of a blunt body in a supersonic gas flow.

1. Experimental setup

The experiments were carried out on the shock tube of the Ioffe Institute [20]. The length of the driver tube is 100 cm, the driven tube is 430 cm, the internal diameter is 50 mm. At the end of the low pressure chamber there is a measuring section with piezoelectric pressure sensors D_1 and D_2 designed by G.N. Suntsov with a working surface diameter of 4 mm and a response time $< 1 \mu\text{s}$. The sensors are installed at a distance of 58 mm from each other and are used to measure the speed of the incident shock wave. The signals were recorded using a Tektronix TDS 2014 oscilloscope with a time resolution of $4 \cdot 10^{-7}$ s. Aluminum diaphragms 0.3 mm thick were used in all experiments. This made it possible to exclude the influence of opening features

on the formation of the shock wave profile and further on the heat transfer processes under study. Therefore, to change the operating modes of the shock tube, the pressure P_1 in the driven tube was varied while the pressure P_4 in the driver tube was unchanged.

In the first series of experiments, the heat flux was measured at the end of the shock tube behind the reflected shock wave. To do this, after the measuring section, an end cap was installed with a pressure sensor D_3 designed by G.N. Suntsov and a thermal sensor H (Fig. 1, a). For a smooth discharge of gas into the damper tank after the experiment, a hole with a diameter of 5 mm was made in the plug. Sensor D_3 was used to register the moment of arrival of the shock wave to the surface of the plug and start recording the sensor signals using a Tektronix TDS 1002 oscilloscope. The temporal resolution was 10^{-8} s with a total duration of $\approx 10 \mu\text{s}$. Thermal sensor H 4×7 mm in size consisted of 10 thermoelements $l = 7$ mm long, $w = 0.4$ mm wide and $h = 0.25$ mm high. According to the stationary calibration data, the volt-watt coefficient was $S_0 = 3.1$ mV/W. The ratio of the length to the thickness of the thermoelement is $l/h = 28$, which allows us to expect the uncertainty of calculating the heat flux from an electrical signal at the level of several percent [21].

In the second series of experiments, the heat flux was measured at the critical point of a blunt body in a supersonic gas flow. To do this, after the measuring section, instead of the end cap, a working chamber was installed, inside which there was a flat supersonic nozzle with an exit section of 40×150 mm, calculated for the Mach number $M = 7$ in the case of a monoatomic gas. A model $40 \times 40 \times 30$ mm was installed in the exit section of the nozzle (Fig. 1, b). Near the middle of the critical line flush with the surface of the model, a thermal sensor H

and a pressure sensor D_3 designed by G.N. Suntsov were installed. Sensor D_3 was used to determine the beginning of the flow and the duration of the steady flow. The signals were recorded using a Tektronix TDS 1002 oscilloscope. The thermal sensor H with the size 3×3 mm consisted of 6 thermoelements $l = 3$ mm long, $w = 0.5$ mm wide and $h = 0.3$ mm thick. The volt-watt coefficient according to the stationary calibration data was $S_0 = 2.7$ mV/W. The smaller ratio $l/h = 10$ compared to the sensor on the end cap will increase the uncertainty of the heat flux calculation from the electrical signal to $\approx 10\%$ [21].

2. Peculiarities of non-stationary heat flow measurement using a sensor on anisotropic thermoelements

When the working surface of the sensor is heated in anisotropic thermoelements, a temperature gradient arises, which leads to the appearance of a thermoelectric field $\mathbf{E}^T = \alpha \nabla T$. Due to the anisotropy of the thermoelectric power α , the direction of the thermoelectric field vector does not coincide with the direction of the temperature gradient. In the general case, the relationship between the distribution of temperature and electric potential in an anisotropic thermoelement is very complex due to the anisotropy of thermal conductivity. For this reason, with the help of numerical simulation, it is possible to solve the direct problem — to calculate the temperature and electric potential field and then the total thermoelectric power from the known heat flux passing through the working surface of the sensor [21–24]. Solution of the inverse problem, i.e. determination of the heat flow from a given thermoelectric power is generally impossible. However, if we consider sensors with the ratio $l/h > 10$, then thermal and thermoelectric processes are described with a sufficient degree of accuracy using a one-dimensional model [21,24]. This greatly simplifies the solution of both direct and inverse problems. In the case of long thermoelements, the main contribution to the total thermoelectric power is made by the transverse component $\Delta\varphi_x$, which can be calculated using the Thomson formula [25]:

$$\Delta\varphi_x = \alpha_{xy} \Delta T \frac{l}{h}, \quad (1)$$

where α_{xy} — off-diagonal element of the thermoelectric power tensor for a given angle of rotation of the crystallographic axes relative to the thermoelement faces, $\Delta T = T_h - T_0$ — temperature difference between the operating and back surfaces. This dependence was obtained at a fixed temperature T_h and T_0 . In this case, the temperature distribution in the main part of the thermoelement is one-dimensional, and the effect of thermal conductivity anisotropy is manifested only near the ends. When anisotropic thermoelements are used as sensitive elements of thermal sensors, the boundary conditions differ from those adopted in the derivation of dependence (1). In

this case, a heat flux passes through the working surface, the back surface is in thermal contact with the substrate, and the side faces are thermally insulated. As heating proceeds, due to the anisotropy of thermal conductivity, the temperature T_h and T_0 along the working and back surfaces changes. The curvature of the isotherms in the thermoelement increases and moves from the ends to the center. When the stationary thermal regime is reached, the isotherms are slanted straight lines [22]. According to relation (1), the thermoelectric power $\Delta\varphi_x$ depends on the temperature difference ΔT , which varies much weaker along the working and back surfaces of the thermoelement, in contrast to the absolute temperature value. Therefore, the errors of the one-dimensional model in the case of using anisotropic thermoelements as sensitive elements of thermal sensors are insignificant [21,24].

In [18] a method for calculating the heat flux passing through the working surface of a single thermoelement, according to a given thermoelectric power, based on dependence (1) is proposed. When using this approach to process the results of measurements using sensors on anisotropic thermoelements, a modification of relation (1) is required to take into account their individual features. After manufacturing, each sensor is calibrated in a stationary thermal mode to determine the volt-watt coefficient $S_0 = U/(q \cdot A)$, where U — electrical signal, q — heat flux density, A — the area of the working surface. Further, substituting the expression for the heat flux $q = -\lambda_{yy}(T_h - T_0)/h$, we can obtain an expression similar to (1), taking into account the parameters of the sensor used:

$$U(t) = \frac{\lambda_{yy} S_0 A}{h} [T_h(t) - T_0(t)], \quad (2)$$

where λ_{yy} — component of the thermal conductivity tensor.

A feature of dependence (2) is the presence of an unknown temperature of the back surface of thermoelements $T_0(t)$ and therefore it must be determined in the process of processing the measurement results. The procedure suggested in [18] can be used for this. The temperature distribution in the thermoelement is found in the course of cyclic solution of the one-dimensional non-stationary heat conduction equation with correction at each iteration of the boundary condition. The boundary condition (3) is set on the working surface of the thermoelement, depending on the electrical signal of the sensor $U(t)$ obtained in the experiment and the temperature of the rear surface $T_0(t)$ found at the previous iteration:

$$T_h^{i+1}(t) = \frac{h}{S_0 \lambda_{yy} A} U(t) + T_0^i(t). \quad (3)$$

The condition $T_0^0(t) = 0$ is used as an initial guess. This algorithm converges because the change in $T_0(t)$ is small compared to the change in $T_h(t)$. The application of the technique for processing the results of measurements showed that to fulfill the condition $|T_h^{i+1}(t) - T_h^i(t)| < 10^{-3}$, it is sufficient several iterations

Table 1. Initial experimental conditions and calculated parameters of nitrogen behind the reflected shock wave

№	P_1 , kPa	P_4 , MPa	M_1	T_5 , K	ρ_5 , kg/m ³	C_{p5} , J/(kg·K)	λ_5 , W/(m·K)
1	4	1.11	2.8	1219	0.489	1203	0.081
2	1.3	1.11	3.1	1412	0.186	1230	0.090
3	0.8	1.11	3.2	1475	0.116	1238	0.094

with a total measurement duration ~ 1 ms. After completion of the iterations, based on the found temperature distribution $T(t)$, it is possible to calculate the heat flux $q_h(t)$ passing through the working surface of the sensor.

3. Heat transfer with the wall behind the reflected shock wave

The main objective of these experiments was to test the method on the process of heat transfer with a wall in the stagnation region behind a reflected shock wave with characteristic time $\sim 1 \mu\text{s}$ and heat flux $\sim 1 \text{ MW/m}^2$. Nitrogen was used as the driver and test gas. Table 1 shows the initial pressure in driven section P_1 and high pressure P_4 , as well as the measured Mach number of the incident shock wave M_1 . Temperature T_5 , density ρ_5 , heat capacity C_{p5} , and thermal conductivity λ_5 of nitrogen behind the reflected shock wave were calculated using Cantera [26] in the approximation of the theory of an ideal shock tube with the real properties of the gases used, represented as polynomials [27]. The initial parameters of the experiments were chosen based on the requirement that the initial composition of the test gas and that heated by the reflected shock wave be identical. The absence of dissociation and ionization significantly simplifies the measurement technique and the calculation of the theoretical value, since the heat flux in this case is determined only by the convective motion of the heated gas.

In accordance with [28], the convective heat flux into the wall behind the reflected shock wave in the absence of dissociation and ionization of the gas and the assumption that the thermal conductivity $\lambda \sim T^\nu$ and the gas density $\rho \sim T^{-1}$ is defined by the expression

$$q(t) = 1.13 \sqrt{\frac{\rho_5 \lambda_5 C_{p5}}{2t}} T_5 \sqrt{\frac{1 - \theta_w^\nu}{\nu} - \frac{1 - \theta_w^{\nu+1}}{\nu + 1}}, \quad (4)$$

where $\theta_w = T_w/T_5$ — the ratio of the wall temperature T_w and the working gas behind the reflected shock wave T_5 , $\nu = 3/4$ — exponent in the law of temperature dependence of gas thermal conductivity.

It can be seen from Table 1 that as the initial pressure in the driven section P_1 decreases, the relative change in the Mach number of the incident shock wave M_1 does not exceed 15%. This leads to a relative change in the

density of the gas behind the reflected shock wave ρ_5 by more than 3 times and with a change in temperature T_5 , heat capacity C_{p5} and thermal conductivity λ_5 by no more than 20%. The parameter that most strongly affects the magnitude of the heat flux under experimental conditions is the gas density ρ_5 behind the reflected shock wave.

Fig. 2, *a* shows the thermal sensor signal recorded in experiment № 1. It can be seen that the noise is present in the signal even before the arrival of the shock wave, which excludes its gas-dynamic nature and is associated with interferences in the recording system. The low signal-to-noise ratio requires preliminary filtering of the original signal before calculating the heat flow. In this case, a Fourier filter with an upper cutoff frequency of 5 MHz was used. According to (2), the thermal sensor signal is proportional to the temperature difference between the working and rear surfaces of the thermoelements $U(t) \sim T_h(t) - T_0(t)$. When the working surface of the sensor with thermoelements 0.25 mm thick is heated, the temperature of the rear surface remains unchanged for $\approx 500 \mu\text{s}$. Therefore, under these conditions, the sensor signal is proportional only to the working surface temperature $U(t) \sim T_h(t)$ (Fig. 2, *b*).

Fig. 3 shows the heat flux calculated from the electrical signal of the sensor for various Mach numbers of the incident shock wave M_1 . High-frequency oscillations are a consequence of the low signal-to-noise ratio of the initial signal of the sensor, which leads to surface temperature oscillations (Fig. 2, *b*), as well as the heat flux calculation method, and do not reflect the real features of heat transfer. At the same time, the low-frequency component is typical for this process: a rapid increase in the initial phase of shock wave reflection and then a slow decrease proportional to $1/\sqrt{t}$, according to (4), due to cooling of the near-wall gas layer.

For a quantitative comparison of experimental and theoretical data, we will consider the quantity $q \cdot \sqrt{t} = \text{const}$, since it depends only on the properties and temperature of the gas behind the reflected shock wave. The $q \cdot \sqrt{t}$ calculated on the basis of experimental data (black line in Fig. 4) reaches a quasi-stationary value during $1 \nu\text{s}$, which demonstrates the sufficient speed of the sensor and the correctness of the method used to calculate the heat flux. The vertical dashed lines show the range of the steady flow over which the averaging was performed. The red line (in the online version) shows the theoretical value calculated from (4).

Table 2 shows the averaged experimental values $\bar{q}_{\text{exp}} \cdot \sqrt{t}$, the theoretical $q_t \cdot \sqrt{t}$ and their relative difference. It can be seen that for all Mach numbers of the incident shock wave, the experimental values are 20–40% less than the theoretical ones. Despite the difference, the obtained results show that the applied method of calculating the heat flux allows obtaining correct results for fast heat transfer processes with a duration of $\sim 1 \mu\text{s}$.

A possible reason for the systematic discrepancy may be the difference between the thermal conductivity λ_{yy} of

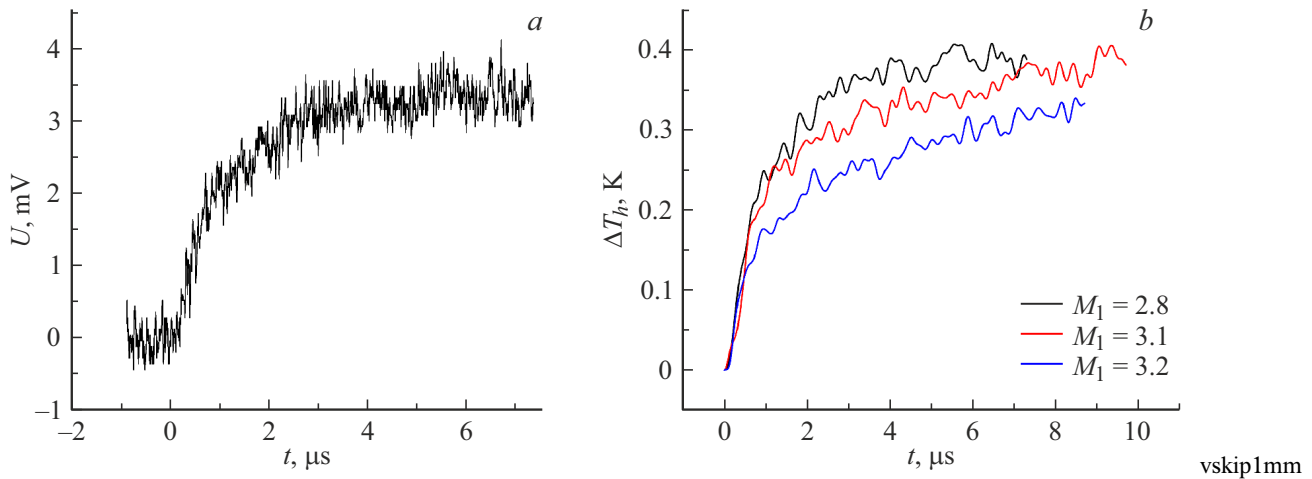


Figure 2. The thermal sensor signal recorded in № 1 (a) experiment and the temperature change of the working surface of thermoelements (b) calculated from (2).

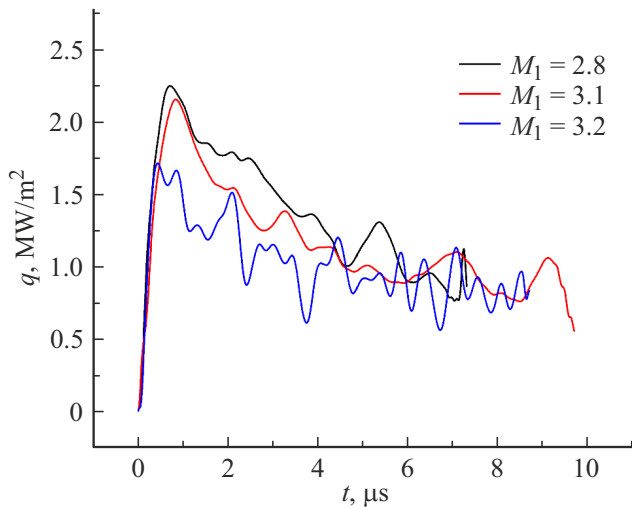


Figure 3. Heat flow into the wall behind the reflected shock wave with different Mach numbers.

a pure bismuth crystal used in the calculation procedure and the effective thermal conductivity in the transverse direction of the anisotropic thermoelements of the sensor used. Other factors cannot explain such a significant discrepancy. The relative uncertainty in measuring the shock wave velocity does not exceed 2%, which leads to uncertainties in calculating the temperature and density of the gas behind the reflected shock wave based on the ideal theory by no more than 3%. The uncertainty in calculating the thermal conductivity coefficient and heat capacity of the gas does not exceed 5%. The final uncertainty of the heat flux calculated by (4) does not exceed 6%. The measurement uncertainty of the volt-watt coefficient of the sensor S_0 , determined during stationary calibration, is 3% [13,14], which is also much less than the obtained value.

Table 2. Time-averaged experimental, theoretical value of $q \cdot \sqrt{t}$ and their relative difference

№	$\bar{q}_{\text{exp}} \cdot t, \text{W} \cdot \sqrt{\text{s}}/\text{m}^2$	$q_t \cdot \sqrt{t}, \text{W} \cdot \sqrt{\text{s}}/\text{m}^2$	$\Delta q/q_t, \%$
1	2342	3948	41
2	2471	3180	22
3	2005	2710	26

4. Heat transfer at the critical point of a blunt body

The main objective of these experiments was to test the methodology on the process of heat transfer at the critical point of a blunt body in a supersonic gas flow with characteristic time $\sim 100 \mu\text{s}$ and heat flux $\sim 100 \text{ kW}/\text{m}^2$. Argon was used as the test gas in order to exclude the effect of gas dissociation and ionization near the critical point and to simplify the measurement and calculation of the theoretical value of the heat flux. Hydrogen was used as a driver gas. Table 3 shows the initial pressure in the driven section P_1 and in the driver section P_4 , the measured Mach number of the incident shock wave M_1 , pressure P_s and stagnation temperature T_s , as well as the degree of dissociation α_{eq} . The pressure, temperature and flow velocity in the nozzle outlet were calculated based on the parameters of the gas behind the reflected shock wave according to the one-dimensional theory. The parameters behind the reflected shock wave were calculated from the initial conditions of the experiments based on the theory of an ideal shock tube, similarly to the previous series of experiments. The degree of argon ionization α_{eq} at temperature T_s and stagnation pressure P_s was calculated using Cantera [26] under the assumption of thermodynamic equilibrium. It should be noted that even for series № 1 with the stagnation temperature $T_s \approx 8000 \text{ K}$,

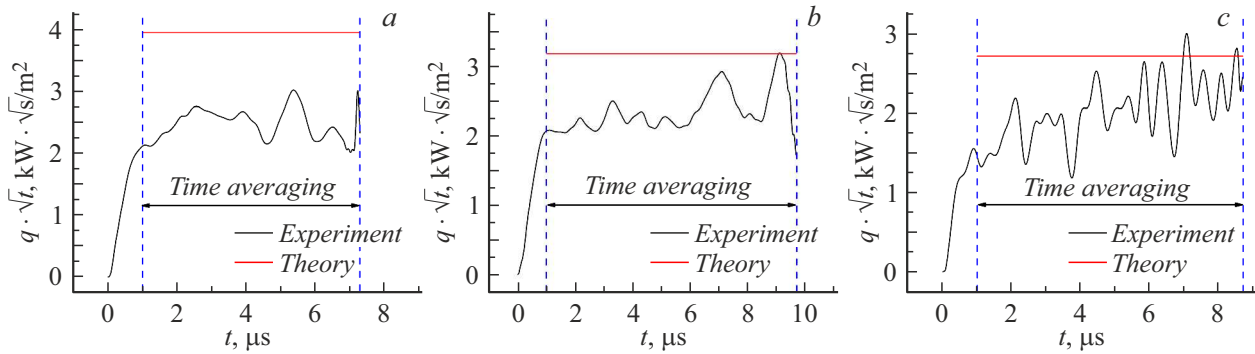


Figure 4. The value of $q \cdot \sqrt{t}$ calculated from the experimental data (black line) and from the dependence (4) (red line (in the online version)) for the Mach numbers of the incident shock waves: $M_1 = 2.8$ (a), 3.1 (b), 3.2 (c).

Table 3. Initial experimental conditions and calculated deceleration parameters of the supersonic argon flow

N ^o	P_1 , kPa	P_4 , MPa	M_1	P_s , kPa	T_s , K	α_{eq}
1	3.3	1.28	6.0	47.6	7970	$3 \cdot 10^{-3}$
2	6.7	1.28	4.7	54.2	4890	$< 10^{-6}$
3	13.3	1.28	4.1	77.8	3710	$< 10^{-6}$

the degree of argon ionization at the stagnation point does not exceed 0.003 and its effect on the heat flux is small. In each series, 4 experiments were carried out.

Fig. 5, a shows the signal of pressure sensor D_3 (red curve (in the online version)) and thermal sensor H (black curve) for one of the experiments of series N^o 1. Time $t = 0$ corresponds to the moment of arrival of the primary shock wave to the surface of the model. Judging by the signal from the pressure sensor, the flow establishment time is $\approx 30 \mu s$. Then, during $\approx 100 \mu s$, there is a period of quasi-stationary flow, which ends at $\approx 130 \mu s$ and is characterized by a rapid increase in pressure. It can be seen that during the test time, marked by vertical dashed lines, the stagnation pressure somewhat increases, which indicates a change in the flow structure near the body. Accordingly, the heat flux at the critical point will also change. For this reason, for comparison with the theoretical value, we will use the heat flux averaged over the test time, obtained in each experiment.

Fig. 5, b shows the electrical signal of the sensor filtered using a Fourier filter with an upper cutoff frequency of 5 MHz. It should be noted that the low signal level, not exceeding 0.2 mV, and the low signal-to-noise ratio, not exceeding 3, led to noticeable uncertainties in the calculation of the heat flux and deviation from the theoretical value.

The theoretical value of the heat flux at the critical point of a blunt body was obtained on the basis of the Fay–Riddell theory [29]. An analysis of the applicability of the theory for monoatomic gases is given in [30]. A simplified expression for the heat flux at the critical point in the absence of gas

dissociation is as follows:

$$q = k(\rho_w \mu_w)^{0.1} (\rho_s \mu_s)^{0.4} (h_s - h_w) \sqrt{\left(\frac{du}{dx}\right)_s}, \quad (5)$$

where k — coefficient describing the shape of the body, ρ_w, μ_w, h_w and ρ_s, μ_s, h_s — density, dynamic viscosity and enthalpy of the gas near the critical point and on the outer boundary of the shock layer, respectively. In the case of a cylindrical body, the coefficient is $k = 0.73$ [31]. The dynamic viscosity of argon was calculated using the Sutherland formula. The velocity gradient at the critical point $\left(\frac{du}{dx}\right)_s$ can be calculated using the expression [32]:

$$\left(\frac{du}{dx}\right)_s = \frac{1}{R} \sqrt{\frac{2(p_s - p_\infty)}{\rho_s}}. \quad (6)$$

Fig. 6 shows the measurement results (colored lines) and the theoretical value of the heat flux (red horizontal line (in the online version)) calculated from (5) for each series of experiments. It can be seen that the behavior of the pressure curve (Fig. 5, a) and heat flux (Fig. 6, b) correlate. The growth of the heat flux during the first $30 \mu s$ corresponds to the phase of the flow around. Further, during $\approx 100 \mu s$, a quasi-stationary flow is observed near the model. It should be noted that the absence of a clear steady-state value of the heat flux in Fig. 6 is a consequence of the low level and filtering of the sensor signal, the need for its mathematical processing, and the short test time of gasdynamic facility in these modes.

Table 4 shows the experimental heat flux \bar{q}_{exp} averaged over the test time calculated according to the Fay–Riddell theory q_{FR} and their relative difference $\Delta q/q_{FR}$. It can be seen that within each series of experiments the averaged value is reproduced and the difference from the theoretical value does not exceed 50%, except for the last experiment. The main factor determining the discrepancy between the theoretical value of the heat flux and the experimental one can be the difference between the parameters of the real supersonic gas flow at the nozzle outlet and those calculated according to the one-dimensional theory (Table 3).

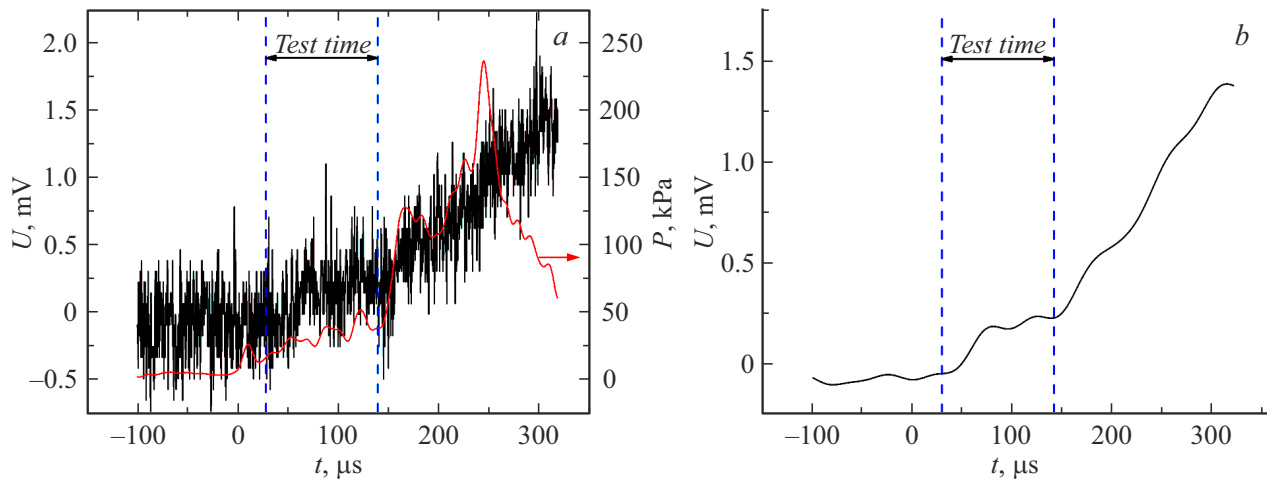


Figure 5. The signal of the thermal sensor H (black curve) and the pressure sensor D_3 (red curve (in the online version)) corresponding to one of the experiments of series № 1 (a); filtered thermal sensor signal (b).

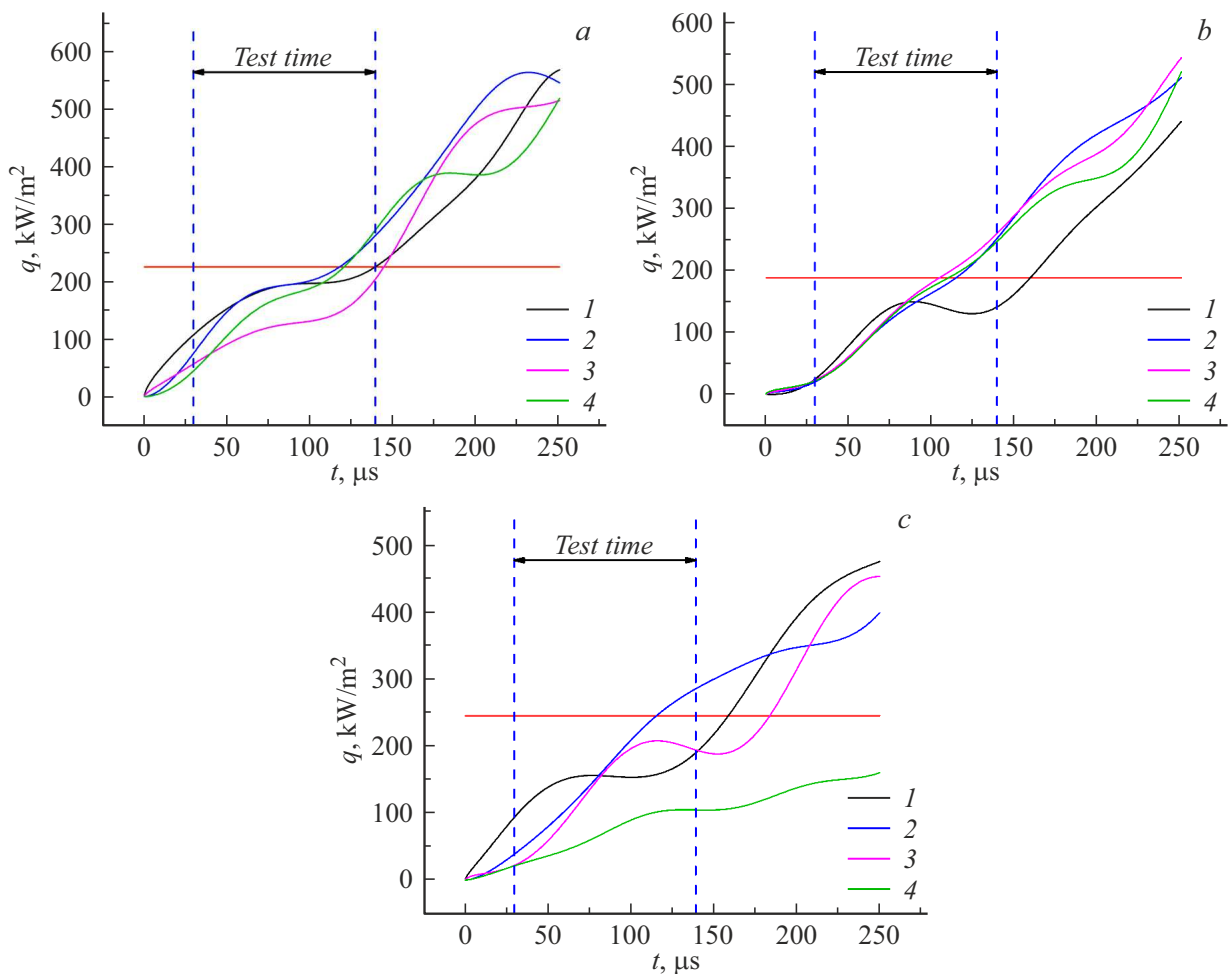


Figure 6. Experimental heat flux for each experiment in series № 1 (a), series № 2 (b), series № 3 (c) and calculated by the Fay–Riddell theory (horizontal line).

Table 4. Heat flux averaged over the time of stationary flow and calculated according to the Fay–Riddell theory, as well as their relative difference

N ^o	\bar{q}_{exp} , kW/m ²	q_{FR} , kW/m ²	$\Delta q/q_{FR}$, %
Series 1			
1	182	226	19
2	190		16
3	124		45
4	169		25
Series 2			
1	117	188	38
2	134		29
3	142		24
4	136		28
Series 3			
1	151	245	38
2	167		32
3	140		43
4	69		71

Conclusion

The features of unsteady heat flux measurements with the help of a sensor on anisotropic thermoelements in experiments on a shock tube are analyzed. The convective heat flux behind the reflected shock wave was measured in nitrogen with Mach numbers $M = 2.8$ – 3.1 and at the critical point of a blunt body in a supersonic argon flow with Mach number $M = 7$. An analysis of the applicability of the developed method for calculating the heat flux from the electrical signal of the sensor under these conditions has been carried out. Possible reasons for the difference between experimental results and theoretical values were analyzed. Despite the noticeable deviations of the measured heat flux from the theoretical value and the absence of a clear stationary region, which are caused by the features of the used gasdynamic facility, the results obtained are qualitatively correct and demonstrate the applicability of the sensor based on anisotropic thermoelements and the signal processing technique in experiments on shock tubes. The calculations presented in [18,21] show that the use of sensors with sufficiently long thermoelements, whose length-to-thickness ratio $l/h > 20$, allows measurements of unsteady heat flux with an uncertainty not exceeding a few percent. Based on the results obtained, it can be affirmed that the developed method for calculating the heat flux from the electrical signal of the sensor based on anisotropic bismuth thermoelements is applicable in a gas-dynamic experiment on pulsed gasdynamic facilities.

Conflict of interest

The authors declare that they have no conflict of interest.

References

- [1] B.R. Hollis, D.K. Prabhu, M. Maclean, A. Dufrene. *J. Thermophys. Heat Transf.*, **31** (3), 712 (2017). DOI: 10.2514/1.T5019
- [2] C.M. James, R. Ravichandran, D.R. Smith, T.G. Cullen, R.G. Morgan. *AIAA Aviation 2020 Forum* (2020), DOI: 10.2514/6.2020-3278
- [3] S.T. Surzhikov. *54th AIAA Aerospace Sciences Meeting* (San Diego, California, USA, 2016), DOI: 10.2514/6.2016-0742
- [4] R. Ferreira, J. Vargas, R. Rodrigues, B. Carvalho, L.L. Alves, B. Goncalves, A. Smith, J. Merrifield, S. McDowell, D. Evans, P. Reynier, V.F. Villace, L. Marraffa. *AIAA Scitech 2020 Forum* (Orlando, Florida, USA, 2020), DOI: 10.2514/6.2020-0624
- [5] V.G. Maslennikov, V.A. Sakharov. *Tech. Phys.*, **42** (11), 1322 (1997). DOI: 10.1134/1.1258870
- [6] C.M. James, B.J.C. Birch, D.R. Smith, T.G. Cullen, T. Millard, S. Vella, Y. Liu, R.G. Morgan, N. Stern, D.R. Buttsworth. *AIAA Aviation Forum* (Dallas, Texas, USA, 2019), DOI: 10.2514/6.2019-3007
- [7] T. Alam, R. Kumar. *Rev. Sci. Instrum.*, **92** (3), 031501 (2021). DOI: 10.1063/5.0015932
- [8] V. Menezes, S. Bhat. *Rev. Sci. Instrum.*, **81** (10), 104905 (2010). DOI: 10.1063/1.3494605
- [9] H. Knauss, T. Roediger, U. Gaisbauer, E. Kraemer, D.A. Bountin, B.V. Smorodsky, A.A. Maslov, J. Srulijes, F. Seiler. *25th AIAA Aerodynamic Measurement Technology and Ground Testing Conference* (San Francisco, California, USA, 2006), DOI: 10.2514/6.2006-3637
- [10] H. Knauss, T. Roediger, D.A. Bountin, B.V. Smorodsky, A.A. Maslov, J. Srulijes. *J. Spacecr. Rockets*, **46** (2), 255 (2009). DOI: 10.2514/1.32011
- [11] M.A. Kotov, A.N. Shemyakin, N.G. Solovyov, M.Yu. Yakimov, V.N. Glebov, G.A. Dubrova, A.M. Malyutin, P.A. Popov, S.A. Poniaev, T.A. Lapushkina, N.A. Monakhov, V.A. Sakharov. *Appl. Therm. Eng.*, **195**, 117143 (2021). DOI: 10.1016/j.applthermaleng.2021.117143
- [12] S.Z. Sapozhnikov, V.Yu. Mityakov, A.V. Mityakov. *Heatmetry: The Science and Practice of Heat Flux Measurement: Heat and Mass Transfer* (Springer International Publishing, 2020)
- [13] S.Z. Sapozhnikov, V.Y. Mityakov, A.V. Mityakov, A.A. Gusakov, E.R. Zainullina, M.A. Grekov, V.V. Seroshtanov, A. Bashkatov, A.Y. Babich, A.V. Pavlov. *Energies*, **13** (23), 6194 (2020). DOI: 10.3390/en13236194
- [14] H. Ozawa. *20th AIAA International Space Planes and Hypersonic Systems and Technologies Conference* (Glasgow, Scotland, 2015), DOI: 10.2514/6.2015-3658
- [15] S.V. Bobashev, N.P. Mende, V.A. Sakharov, D.M. van Wie. *42nd AIAA Aerospace Sciences Meeting and Exhibit* (Reno, Nevada, USA, 2004), DOI: 10.2514/6.2004-515
- [16] S.V. Bobashev, N.P. Mende, V.A. Sakharov, S.Z. Sapozhnikov, V.Yu. Mityakov, A.V. Mityakov, D.M. Van Wie. *43rd AIAA Aerospace Sciences Meeting and Exhibit* (Reno, Nevada, USA, 2005), DOI: 10.2514/6.2005-787
- [17] S.V. Bobashev, N.P. Mende, V.A. Sakharov, S.Z. Sapozhnikov, V.Yu. Mityakov, A.V. Mityakov, D.M. Van Wie. 2007, *45th AIAA Aerospace Sciences Meeting and Exhibit* (Reno, Nevada, USA, 2007), DOI: 10.2514/6.2007-220

- [18] P.A. Popov, S.V. Bobashev, B.I. Reznikov, V.A. Sakharov. *Tech. Phys. Lett.*, **44** (4), 316 (2018).
DOI: 10.1134/S1063785018040235
- [19] Y.V. Dobrov, V.A. Lashkov, I.Ch. Mashek, A.V. Mityakov, V.Yu. Mityakov, S.Z. Sapozhnikov, R.S. Khoronzhuk. *Tech. Phys.*, **66** (2), 229 (2021).
DOI: 10.1134/S1063784221020109
- [20] S.V. Bobashev, A.V. Erofeev, T.A. Lapushkina, S.A. Poniaev, R.V. Vasil'eva, D.M. Van Wie. *J. Propuls. Power*, **21** (5), 831 (2005). DOI: 10.2514/1.2624
- [21] P.A. Popov, S.V. Bobashev, B.I. Reznikov, V.A. Sakharov. *Tech. Phys. Lett.*, **43** (4), 334 (2017).
DOI: 10.1134/S1063785017040125
- [22] S.V. Bobashev, P.A. Popov, B.I. Reznikov, V.A. Sakharov. *Tech. Phys. Lett.*, **42** (5), 460 (2016).
DOI: 10.1134/S1063785016050035
- [23] P.A. Popov, S.A. Poniaev, V.A. Sakharov, B.I. Reznikov, N.A. Monakhov. *J. Phys.: Conf. Ser.*, **1697**, 012227 (2020).
DOI: 10.1088/1742-6596/1697/1/012227
- [24] P.A. Popov. *J. Phys.: Conf. Ser.*, **2103**, 012215 (2021).
DOI: 10.1088/1742-6596/2103/1/012215
- [25] D.M. Rowe. *Thermoelectrics Handbook: Macro to Nano* (CRC Press, 2006)
- [26] [Electronic source] Available at: Cantera. <https://cantera.org/> (Checked on 04/03/2022)
- [27] B.J. McBride, M.J. Zehe, S. Gordon. *NASA Glenn Coefficients for Calculating Thermodynamic Properties of Individual Species* (NASA/TP/2002-211556, 2002)
- [28] J.A. Fay, N.H. Kemp. *J. Fluid Mech.*, **21** (4), 659 (1965).
DOI: 10.1017/S002211206500040X
- [29] J.A. Fay, F.R. Riddell. *J. Aerosp. Sci.*, **25** (2), 73 (1958).
DOI: 10.2514/8.7517
- [30] J.P. Reilly. *Phys. Fluids*, **7** (12), 1905 (1964).
DOI: 10.1063/1.1711099
- [31] F. White, J. Majdalani. *Viscous Fluid Flow* (McGraw-Hill, 2021)
- [32] Z. Ilich, G. Grossir, O. Chazot. *33rd AIAA Aerodynamic Measurement Technology and Ground Testing Conference* (Denver, Colorado, USA, 2017), DOI: 10.2514/6.2017-3984